J Mater Sci (2019) 54:10270–10283

Computation and theory

Modelling and analysis of the oxide growth coupling behaviour of thermal barrier coatings

Xiaokang Wang[1], Xueling Fan[1,*], Yongle Sun[2], Rong Xu[1], and Peng Jiang[1]

[1] State Key Laboratory for Strength and Vibration of Mechanical Structures, School of Aerospace Engineering, Xi'an Jiaotong University, Xi'an 710049, China

[2] School of Mechanical, Aerospace and Civil Engineering, The University of Manchester, Sackville Street, Manchester M13 9PL, UK

Received: 3 January 2019
Accepted: 10 April 2019
Published online: 16 April 2019

ABSTRACT

A chemo-transport-mechanics model is developed to study the growth of thermally grown oxide (TGO) and its impact on deformation and stress in air plasma-sprayed thermal barrier coatings (TBCs). As the driving force for oxygen transport, the chemical potential consists of contributions from both species concentration and hydrostatic pressure. The model suggests that both the concentration boundary condition and the transport process of the oxygen are affected by hydrostatic stress. Since oxygen has smaller diffusion coefficient in TGO than in BC, the retarding effect of the formed TGO on oxygen transport is considered and clarified by the coupled model. The competition between geometrical imperfection (i.e. concave morphology) and the chemo-mechanics coupling to influence the transport of oxygen is also identified numerically. The geometrical imperfection can introduce additional oxygen transport at the margin of the concave imperfection due to the horizontal component of the gradient of the chemical potential of the oxygen, which plays a dominant role in the TGO growth kinetics for the studied TBCs. Consequently, there is a limited effect of the chemo-mechanics coupling on the growth kinetics of a concaved TGO. The amplitude change of the concave portion is found to be up to 0.36 μm after 600-h exposure at 1150 °C, which leads to large tensile stress above the concave portion potentially causing micro-cracks.

Address correspondence to E-mail: fanxueling@mail.xjtu.edu.cn

https://doi.org/10.1007/s10853-019-03620-7

List of symbols

σ	Hydrostatic stress
σ_{ij}	Stress component
ε_{ij}	Strain component
K_{ijkl}	Stiffness matrix
ε_{ij}^{e}	Elastic strain
ε_{ij}^{p}	Plastic strain
ε_{ij}^{T}	Thermal strain
ε_{ij}^{g}	Growth strain
ε_{ij}^{c}	Chemical strain
u_i	Displacement
α	Coefficient of thermal expansion (CTE)
T	Temperature
T_0	Reference temperature
R_{PB}	Pilling–Bedworth ratio
ξ	Oxide volume percentage
c	Oxygen concentration
Ω	Partial molar volume
μ	Chemical potential
μ_0	Reference chemical potential
R	Gas constant
J	Diffusion flux
D	Diffusion coefficient
D_0	Reference diffusion coefficient
$H(\xi)$	Step function
v	Chemical reaction rate
K	Chemical reaction constant
r_{D}	Ratio of diffusion coefficient of oxygen in TGO to that in BC

Introduction

Enhancing efficiency of gas turbine engine demands the increase in temperature of inlet gas, which, however, is difficult to achieve by solely using superalloy as the constituent material of turbine blades, since most superalloys have limited thermal resistance which is insufficient for extreme temperatures. Thermal barrier coatings (TBCs) are widely used as a thermal insulator to protect the turbine blades from the high-temperature environment due to their excellent thermal resistance [1–6]. Typically, TBCs consist of a ceramic top coat (TC), a thermally grown oxide (TGO) layer and a metallic bond coat (BC) deposited on the superalloy substrate. Among these components, TGO plays a critical role in the mechanical integrity and service life of TBCs. TGO can form during both fabrication and service, as oxygen inevitably diffuses through porous TC and reacts with metallic BC at high temperature. TGO thickness increases as the oxidation proceeds, accompanied by the formation of new oxides both along the inner grain boundary of TGO and at the TGO–BC interface, causing a lateral growth strain and a through-thickness growth strain, respectively [1, 2, 7, 8].

The effect of TGO growth on the performance and service life of TBCs has been extensively studied in prior works which are mainly focused on the mechanical point of view such as the strain-energy-driven failure induced by TGO growth [1, 2, 9–16]. As the thickness of TGO increases during high-temperature exposure, micro-cracks form in the TBCs around the imperfections at interface because of the mismatch strain [17–19]. TGO thickening at a given gas temperature could be predicted using either an empirically parabolic formula or a diffusion–reaction model. These predictions are useful and necessary to evaluate the stress field generated by the TGO thickening and the associated mechanical failure within TBCs [20–22]. Previous studies [17, 22–28] have shown that the TGO displacement instability, which initiates large cracks and causes failure of TBCs, is more likely to develop in regions where micro-cracks either pre-exist or are caused by in-service stress.

While the mechanical failures induced by the TGO growth are relatively well understood, the chemo-mechanics coupling mechanisms governing the growth of TGO are obscure and have been less explored. The growth of TGO involves the complicated couplings such as the couplings between the concurrent stress evolution, oxygen diffusion and oxidation reaction [2]. Zhou et al. [29] studied the reactive element effect on the modification of cation diffusivity in oxide scale, assuming that the oxidation reaction is at equilibrium state. Based on thermodynamics and continuum mechanics, Loeffel et al. [30, 31] established a highly nonlinear and coupled model to describe and analyse the diffusion of oxygen, oxidation reaction, elastic-viscoplastic deformation and heat conduction in the high-temperature oxidation of superalloy. Lin et al. [32] further modified the model proposed by Loeffel et al. by including the chemical potential balance of oxygen at solid–gas interface. Suo and Shen [33] also developed a coupled diffusion–reaction mechanics model to investigate the oxidation of metallic plate with consideration of the effect of hydrostatic stress on the chemical

Table 1 Theoretical models of TGO growth

Model	Chemo-mechanical coupled		Decoupled	
	Anion diffusion dominated	Cation diffusion dominated	BC changed to TGO	TGO thickness increase
Sphere	–	–	[45]	[7, 8, 23]
Beam/plate	–	[37–39]	[40, 41]	[42]
Cylinder	–	–	[43, 44]	[7]
Complex configuration	[31–33]	[30]	–	[36]

potential of oxygen. Several theoretical models of TGO growth are reviewed in Table 1 [34]. For coupled models, the inward anion and/or outward cation diffusion is taken into consideration. The process with higher diffusivity dominates the oxidation reaction. For decoupled models, two distinct ways are developed. In some models, the material properties are changed from those of BC to those of TGO, representing the material change caused by oxidation reaction. Others either add growth strains to or increase the thickness of the TGO layer without explicitly accounting for material change.

These previous models are valuable for us to gain general insights into the stress evolution during the oxidation process. However, the decoupled models require the TGO growth rate as an input. While predicting the growth rate theoretically is possible using some models (e.g. Loeffel et al. [30, 31]), it requires material parameters that are difficult to experimentally measure, significantly limiting the application of these models in engineering design and analysis. In addition, while it is widely recognised that the diffusivity of oxygen in BC differs significantly from that in TGO [1, 2], this phenomenon is mostly ignored in the models summarised in Table 1.

In this paper, we develop a chemo-transport-mechanics model to simulate the TGO growth coupling behaviour and the retarding effect of formed oxide on the diffusion of oxygen. The influence of stress on chemical potential is considered, and the factors affecting the oxidation process, especially the diffusion coefficient of oxygen, are discussed. Furthermore, the displacement instability of TGO with a pre-existing concave imperfection and the TGO growth-induced stress are predicted and analysed.

Coupled chemo-transport-mechanics model

We assume the deformation of TBCs during operation is small such that the strain can be written in terms of the displacement field u as

$$\varepsilon_{ij} = \frac{1}{2}\left(u_{i,j} + u_{j,i}\right). \tag{1}$$

During the oxidation, the strain of TGO can be decomposed into the following components

$$\varepsilon_{ij} = \varepsilon_{ij}^{e} + \varepsilon_{ij}^{p} + \varepsilon_{ij}^{T} + \varepsilon_{ij}^{g} + \varepsilon_{ij}^{c}, \tag{2}$$

where ε_{ij}^{e}, ε_{ij}^{p}, ε_{ij}^{T}, ε_{ij}^{g} and ε_{ij}^{c} represent the elastic, plastic, thermal expansion, TGO growth and chemical expansion strains, respectively. Note that (1) the elastic and plastic strains are associated with mechanical response; (2) the thermal expansion strain is caused by temperature change; (3) TGO growth strain arises from oxidation; and (4) chemical expansion strain is induced by oxygen diffusion.

Since the residual stress induced during material fabrication can be largely released at elevated temperatures, we assume that the system before oxidation is stress-free. The constitutive equation for an isotropic and homogeneous material can be expressed as follows:

$$\sigma_{ij} = K_{ijkl} : \varepsilon_{kl}^{e}, \tag{3}$$

where σ_{ij}, K_{ijkl} and ε_{kl}^{e} are stress components, stiffness matrix and elastic strain components, respectively. The thermal strain is given by

$$\varepsilon_{ij}^{T} = \alpha(T - T_0)\delta_{ij}, \tag{4}$$

where α is coefficient of thermal expansion (CTE), T is temperature, and T_0 is a reference temperature for strain-free condition.

Growth strain is defined as an isotropic expansion strain determined by volume change after oxidation:

$$\varepsilon_{ij}^{g} = \left(\sqrt[3]{R_{\mathrm{PB}}} - 1\right)\xi\delta_{ij}, \tag{5}$$

where R_{PB} is the Pilling–Bedworth ratio [45] and ξ is the volume percentage of the oxide which ranges from 0 to 1 during the oxidation.

Chemical strain describes the expansion of the oxygen dissolution, and it is defined as follows [35]:

$$\varepsilon_{ij}^{c} = c\Omega\delta_{ij}, \tag{6}$$

where c and Ω are oxygen concentration (mol/m^3) and partial molar volume (m^3/mol), respectively.

The stress equilibrium equation is given by

$$\sigma_{ij,j} + f_i = 0 \tag{7}$$

where f_i is the body force.

For simplicity, a rule of mixtures is adopted to determine the stiffness of the partially oxidised BC, i.e.

$$K = (1-\xi)\cdot K_{BC} + \xi K_{TGO}, \tag{8}$$

where K_{BC} and K_{TGO} are stiffness matrix for BC and TGO, respectively.

Since TC is porous and inactive with oxygen, the barrier to oxygen diffusion within TC layer can be neglected. The oxidation proceeds as the oxygen diffuses inward through formed TGO and reaches the reaction front where the oxygen meets the aluminium contained in BC, and the oxide, α-alumina, is formed at the stable oxidation stage [1–3]. Based on thermodynamics, the chemical potential μ in an ideal solid solution can be expressed as [45]:

$$\mu = \mu_0 + RT\ln(c/c_0) - \sigma_m\Omega, \tag{9}$$

where μ_0, R, T, c, c_0 and σ_m are chemical potential at reference state, universal gas constant, absolute temperature, oxygen concentration, reference concentration and hydrostatic pressure, respectively. If the last term $\sigma_m\Omega$ vanishes, the model reduces to the classical, non-coupling model. Chemical potential serves as the driving force of diffusion. In quasi-equilibrium state, the diffusion flux J can be obtained by [46]:

$$J = -\frac{Dc}{RT}\nabla\mu, \tag{10}$$

where D (m^2/s) is the diffusion coefficient of oxygen.

The Reynolds transport theorem [47] requires that the rate of the variation of a chemical species is equal to the sum of the flux and the source, i.e.

$$\dot{c} = -\nabla\cdot J - v, \tag{11}$$

where $\dot{c}$ and v denote variation rate and chemical reaction rate, respectively.

For simplicity, when dealing with the chemical reaction equation, only the first-order reaction is considered. According to Guldberg–Waage law of mass action [48], the rate of the first-order chemical reaction v can be expressed as follows:

$$v = kc(1-\xi), \tag{12}$$

where k is a constant, independent of temperature and concentration of oxygen.

We assume that oxide does not exist in the beginning and confine the scope to the initial stable oxidation process when α-Al_2O_3 is the only oxide [49], as shown in Fig. 1. The volume percentage of oxide is calculated as the ratio of number of metallic atoms in oxides to the number of all the metallic atoms in the layer. The oxidation front moves forward as the volume percentage of the oxide increases. During the time interval between t and $t+\delta t$, the consumption of oxygen ion for a given volume, δV, follows the relation that $\delta N_O = v\delta V\delta t$. Therefore, the associated change of ξ can be expressed as follows,

$$\delta\xi = \frac{\delta N_O}{N} = \frac{v\delta V\delta t}{N\delta V}. \tag{13}$$

Equation (13) can be rewritten as

$$\dot{\xi} = \frac{\delta\xi}{\delta t} = \frac{v}{N}, \tag{14}$$

where N is the concentration of the aluminium ion at the given area. Solving the differential equation with an initial condition that $\xi|_{t=0} = 0$, we obtain

$$\xi = 1 - \exp\left(-\frac{kct}{N}\right). \tag{15}$$

Combining Eqs. (1), (3), (7), (11) and (15), the chemo-transport-mechanics coupling model is established, as follows:

$$\varepsilon_{ij} = \frac{1}{2}\left(u_{i,j} + u_{j,i}\right), \tag{16}$$

$$\sigma_{ij,j} = 0, \tag{17}$$

$$\sigma_{ij} = K_{ijkl} : \varepsilon_{kl}^{e}, \tag{18}$$

$$\dot{c} = -\nabla\cdot J - v, \tag{19}$$

$$\xi = 1 - \exp\left(-\frac{kct}{N}\right). \tag{20}$$

The commercial software COMSOL is used to numerically solve these equations. Note that for the benefit of convergence, Eq. (19) is multiplied by a test

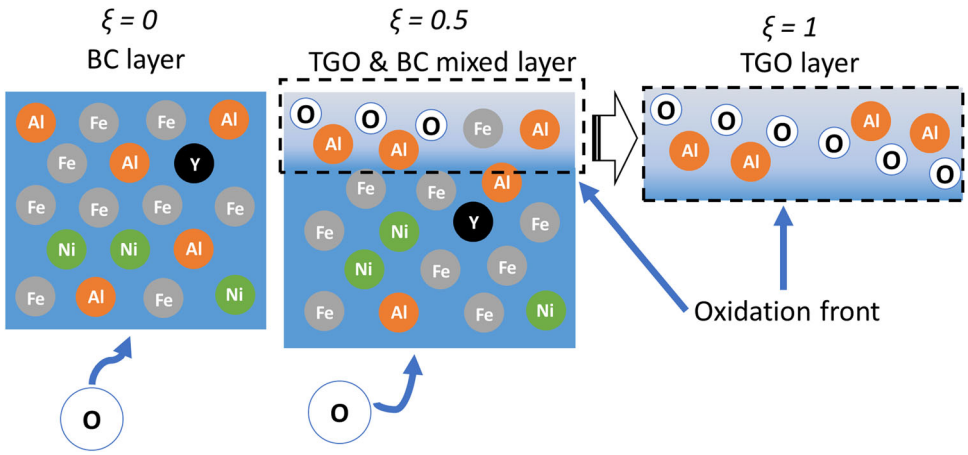

Figure 1 Schematics of the oxidation process occurring in a representative oxidation site. Both aluminium and oxygen ions diffuse into the oxidation site (blue block), while the other metallic ions such as Ni^{3+} and Fe^{3+} diffuse from the oxidation site to the cavity in the BC layer.

function and integrated over the volume of the material in order to obtain a weak coupling form, i.e.

$$\int_V (\dot{c} + \nabla \cdot J + vc)\hat{\mu} \mathrm{d}V = 0, \tag{21}$$

where $\hat{\mu}(x_i, t)$ is a test function which vanishes on the boundary. Integrating above equation by parts, we obtain

$$\int_V [(\dot{c} + vc)\hat{\mu} - J \cdot \nabla \hat{\mu}] \mathrm{d}V + \int_{\partial V} n \cdot J \hat{\mu} \mathrm{d}S = 0. \tag{22}$$

Also note that here the chemical potential field, rather than the concentration field, is calculated to speed up the convergence. Then the concentration is obtained by

$$c = c_0 \cdot \exp[(\mu - \mu_0 + \sigma_m \Omega)/RT], \tag{23}$$

The same procedure is adopted for Eq. (17) which leads to

$$\int_V \boldsymbol{\sigma} \cdot \nabla \boldsymbol{u} \, \mathrm{d}V - \int_V \boldsymbol{F_b} \cdot \boldsymbol{u} \, \mathrm{d}V - \int_{\partial V} \boldsymbol{P} \cdot \boldsymbol{u} \, \mathrm{d}V = 0, \tag{24}$$

where $\boldsymbol{\sigma}$, $\boldsymbol{u}$, $\boldsymbol{F_b}$, $\boldsymbol{P}$ denote stress tensor, test function, body force and surface traction, respectively.

Numerical simulation scheme

We implement the chemo-transport-mechanics theory described in "Numerical simulation scheme" Section into finite element model (FEM), which is particularly efficient to investigate the effect of stress–oxidation coupling on the evolutions of stress field and oxygen distribution. As aforementioned, the pristine TBCs consist of three layers with geometrical imperfections at TC–BC interface, see Fig. 2a. An upward concave interface is used to represent a typical imperfection [7–9]. The geometrical parameters are listed in Table 2. Note that while curvature of the imperfection could affect the result, we use the simplified geometry to elaborate a representative case. We employ an axisymmetry assumption for the TBCs model and refine the mesh near TC–BC interface.

We set the following mechanical and chemical boundary conditions. The displacement along axial direction (z) at the bottom is constrained, and the displacement along radial direction (r) at the right side is also constrained. The temperature rises from room temperature to T (see specified values in the discussion in Sect. 4) in 2 min and then is kept constant. TC and BC are initially closely packed, and then TGO keeps forming along TC–BC interface during the oxidation. The lower and right sides of BC layer are assumed to be oxygen insulated, while the upper side is applied by a chemical potential that satisfies the atmosphere condition [32],

$$\mu_0 + RT \ln \frac{c}{c_0} - \sigma_{\mathrm{m}} \Omega = \frac{1}{2}\left(\mu_{0,O_2} + RT \ln \frac{p_{O_2}}{p_0}\right). \tag{25}$$

The FE model has 4275 quadrilateral elements and 1685 triangle elements, with the minimum element size of 0.15 μm, as shown in Fig. 2b. The mesh sensitivity has been examined, confirming that the current mesh is fine enough to obtain converged results. The first- and second-order shape functions are adopted for calculating the chemical potential and displacement fields, respectively. The fully coupled solver is used to guarantee the accuracy.

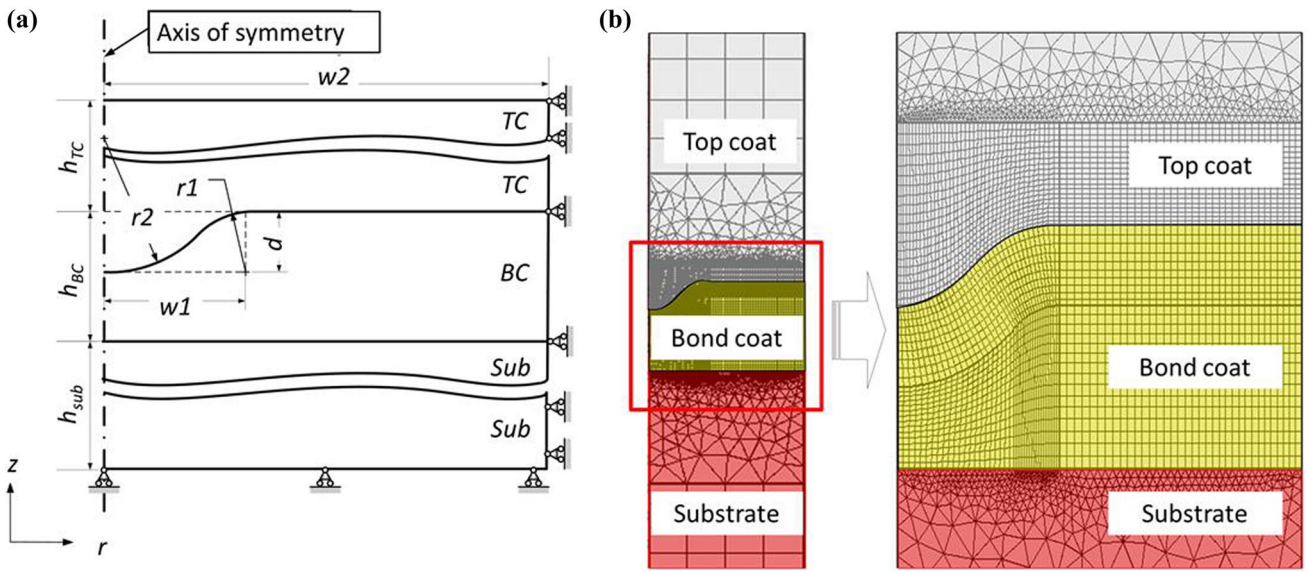

Figure 2 **a** Sketch of the FE model of TBCs; **b** details of the FE mesh.

Table 2 Geometrical parameters

Parameters	Value
$w1$	15 μm
d	8 μm
$r1$	8 μm
$r2$	$(d^2 + w1^2/4)/2d - r1$
$w2$	25 μm
h_{TC}	150 μm
h_{BC}	80 μm
h_{sub}	2000 μm

Table 3 Thermodynamic parameters [31, 32, 51]

Parameter	Value
Ω (m^3 mol^{-1})	1.56×10^{-6}
R (J mol^{-1} K^{-1})	8.3144598
D_0 (m^2 s^{-1})	1×10^{-12}
p_{O2} (MPa)	0.021
p_O (MPa)	0.1
μ_0 (KJ mol^{-1})	112
N (m^3 mol^{-1})	0.24×10^6
c_0 (m^3 mol^{-1})	0.08×10^6
ξ_0	0.8

Elastic–plastic behaviour is considered for both BC and TGO. The strain hardening modulus is taken to be 5% of Young's modulus [50]. Thermodynamic parameters used in simulation are listed in Table 3. Temperature-dependent material properties of ceramic top coat, TGO (Al_2O_3), BC (FeCrAlY alloy), and superalloy substrate are summarised in Tables 4, 5, 6 and 7, respectively. Note that the rule of mixtures as described in Eq. (8) is adopted for BC layer.

Results and discussion

Diffusion barrier effect on TGO growth kinetics

The oxygen typically diffuses at different rates within the BC and the oxidation product, i.e. alumina. The relatively slow kinetics of oxygen diffusion in oxidation product significantly influences the TGO formation and growth, which is usually referred to as the diffusion barrier effect of oxidation product. However, most previous studies ignore this diffusion barrier effect by simply assuming a constant oxygen diffusivity for both BC and oxidation product. In this section, we investigate how the slow oxygen diffusion in oxidation product affects the TGO formation and growth.

The formation of TGO is usually simulated with varying k [32] in Eq. (11), which can be used to evaluate the oxygen diffusion effect on TGO growth kinetics. Here the simulation was carried out using the numerical model described in "Results and discussion" section at T = 1070 °C, which is the same as that in the experiment [54]. The results shown in Fig. 3 are obtained by setting k as a constant and by

Table 4 Material parameters of BC (FeCrAlY alloy) [52]

Temperature (K)	293	493	693	893	1093	1293
Young's modulus (GPa)	220	205	190	170	150	150
Poisson's ratio	0.28					
Coefficient of thermal expansion (10^{-6} K^{-1})	10.0	11.1	12.0	13.5	14.0	15.0
Yield strength (MPa)	310	240	170	120	35	35

Table 5 Material parameters of TGO (Al_2O_3) [32, 52]

Temperature (K)	293	493	693	893	1093	1293
Young's modulus (GPa)	375	360	350	345	340	340
Poisson's ratio	0.28	0.28	0.28	0.3	0.32	0.37
Coefficient of thermal expansion (10^{-6} K^{-1})	5.5	7.3	8.1	8.7	9.3	9.6
Yield strength (GPa)	10	10	10	10	10	1

Table 6 Material parameters of top coat (APS ZrO_2-8%Y_2O_3) [53]

Temperature (K)	293	493	693	893	1093	1293	1393
Young's modulus (GPa)	48	47	44	40	34	26	22
Poisson's ratio	0.10	0.10	0.10	0.11	0.11	0.12	0.12
Coefficient of thermal expansion (10^{-6} K^{-1})	9.0	9.2	9.6	10.1	10.8	11.7	12.2

Table 7 Material parameters of substrate (PWA 1480 alloy) [53]

Temperature (K)	293	493	693	893	1093	1293	1393
Young's modulus (GPa)	220	210	190	170	155	130	120
Poisson's ratio	0.31	0.32	0.33	0.33	0.34	0.35	0.35
Coefficient of thermal expansion (10^{-6} K^{-1})	14.8	15.2	15.6	16.2	16.9	17.5	18.0

altering k during the oxidation process according to a step function which decreases from 15 to 1, after 100 h from the oxidation process. In both cases, the TGO shows a quasi-parabolic growth rate. If k is kept as a constant, large discrepancy between prediction and experimental result is found, either at the beginning or at the final period of the oxidation process. Furthermore, TGO thickness is insensitive to k for all $k > 9$. If k changes according to the step function mentioned above, the prediction of the TGO thickness agrees well with the experimental observation [54]. These results suggest that a constant k in modelling is not a good assumption which does not reflect the reality. The reason for the variation in k during TGO growth lies in the difference of the reaction between the beginning and the end of the

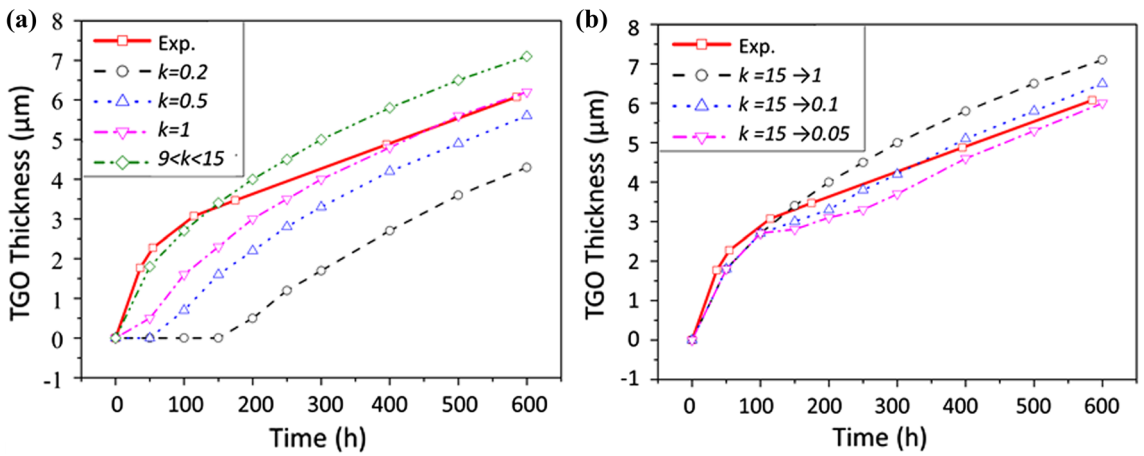

Figure 3 Predictions of TGO thickness when different values of k are considered: **a** k is a constant during the oxidation process; **b** k varies with oxidation time. Experimental data are extracted from a prior work [55].

oxidation process. Note that the change in k above is empirical and it does not explicitly take into account the diffusion barrier of the formed oxide.

Since the diffusivity of oxygen in the BC layer is far higher than that in alumina layer, the oxygen can quickly diffuse through the BC and reach the reaction front at the early oxidation process, resulting in a fast formation of alumina layer (i.e. TGO). As the oxidation proceeds, the TGO keeps growing and its thickness increases. The slow kinetics of oxygen diffusion in the thick TGO layer could prevent the oxygen ions from further reaching the fresh reaction front of TGO layer and thus reduce the oxidation rate at the later stage of initial stable oxidation process. To capture this diffusion barrier effect on the TGO growth, we assume that the oxygen diffusivity D in TGO layer is dependent on the oxide fraction ξ, as the relation $D = D_0 \cdot H(\xi - \xi_0)$. D_0 is the oxygen diffusivity in BC layer, and $H(\xi - \xi_0)$ is a step function defined as

$$H(\xi - \xi_0) = \begin{cases} 1, & \xi \geq \xi_0 \\ r_D, & \xi < \xi_0 \end{cases}. \quad (26)$$

The ξ_0 in Eq. (26) is the critical oxide fraction used to separate the BC and TGO, below which the BC layer is still at pristine state such that the oxygen diffusivity is taken as D_0, and above which the BC layer has been oxidised into TGO such that the oxygen diffusivity is taken as $D = r_D D_0$. Here r_D is the ratio of oxygen diffusivities in BC and TGO.

Here we study the diffusion barrier effect of the formed oxide by holding the D_0 as a constant and changing the r_D. The reaction constant k is set to be 15 [32]. Figure 4 shows the TGO thickness as a function of oxidation time for various r_D. Again, for all the cases, the thickness of the TGO keeps increasing while the increasing rate decays. Specifically, the TGO growth behaviour for $r_D = 0.75$ is in good agreement with the experimental result. This agreement implies that the low diffusion coefficient of oxygen in TGO indeed plays an important role in the oxidation process, as discussed in last paragraph. $r_D = 0.75$ is taken as the benchmark in the following analyses in "Stress-regulated oxygen diffusion in TBCs" and "Stress-regulated morphology of TGO layer" sections. Note that the above simulation could be used to determine the relative ratio of the oxygen diffusivities in BC and TGO, which is also applicable to other material systems like the oxidation of silicon in environmental barrier coatings [55].

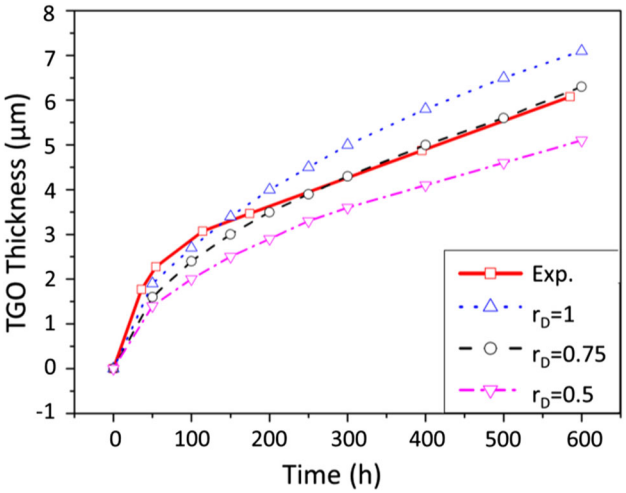

Figure 4 TGO thickness versus time. Variation in diffusion coefficient is considered in modelling.

Stress-regulated oxygen diffusion in TBCs

In this section, we study the chemo-mechanics coupling on the basis of two sets of simulations. In Set I, all the material properties are set to be independent of the oxide fraction ξ. In Set II, material properties for the region that is gradually oxidised from BC to TGO are assumed to follow the mixture rule. The oxide fraction ξ is the only parameter determining the mixed material properties.

$$X = (1 - \xi) \cdot X_{\mathrm{BC}} + \xi \cdot X_{\mathrm{TGO}} \ (X = E, \upsilon, \alpha, D, \sigma^{Y}). \quad (27)$$

As shown in Fig. 5a, the red colour in the upper part indicates very high volume percentage of oxygen. Oxidation at this region is suppressed due to the absence of metal atoms. The oxygen is then transported to the oxidation front where reaction rate is a maximum due to the abundance of both oxygen and metal atoms. Beyond the oxidation front, oxygen concentration decays quickly and the percentage of oxide is very low. Figure 5b, c shows the TGO thickness at the flat region as a function of time. It is clear that (1) the thickening trend is consistent with the classic parabolic law; (2) the TGO thickness of the coupling model is slightly smaller, compared to the non-coupling model wherein the chemical potential is independent of the stress; and (3) TGO thickness predicted from Set I is larger than that of Set II. The results here indicate that in Set II, as the material

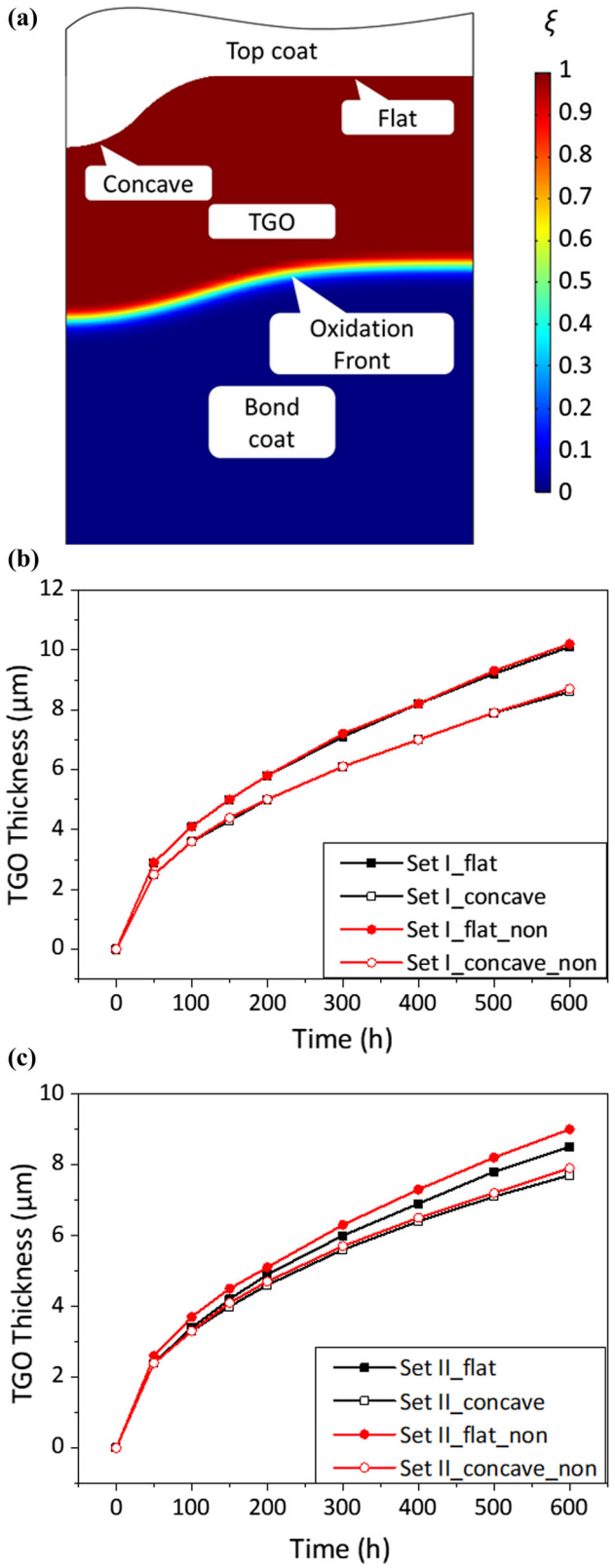

Figure 5 TGO thickness evolution. "Concave" and "flat" in (**b**) and (**c**), respectively, correspond to the location shown in (**a**). The subscript "non" indicates non-coupling model.

changed from pure BC to a mixture, the TGO thickening process is retarded. In the following sections, we will only focus on Set II as it is more realistic.

Apart from the parabolic-like thickening trend, the TGO thickness is different at different locations, namely the centre of the concave, the marginal region of the concave and the flat region. Two factors account for this feature. The first is the hydrostatic stresses near the interface of TGO and TC, which influences the boundary condition of oxygen concentration, according to Eq. (25). This boundary condition determines the supply of the oxygen and influences the oxidation process. The second is that the stress regulates the diffusion of the oxygen, since the chemical potential drives the oxygen from the compression region to the tensile region, according to Eq. (23).

Figure 6a shows the hydrostatic stress near the interface of TGO and TC. Two key features can be identified. First, the hydrostatic stress changes from tension at the centre of the concave to compression as it gets away from the concave for both coupling and non-coupling cases. Large volume expansion around the concave due to TGO growth strain causes mismatch strain around the imperfection. The mismatch strain in turn leads to the tension at the concave region, and compression in regions away from the imperfection. At 600th hour after oxidation, the maximum compressive stress occurs at the junction of the concave. Second, the coupling case shows much higher tensile hydrostatic stress than the non-coupling case, which implies that cracks may initiate locally due to the large tensile stress. Figure 6b plots the oxygen concentration at the upper boundary of TGO (pristine TC–BC interface) and TGO thickness distribution along the interface after 600 h. For coupling case, the oxygen concentration is higher in concave region. The concentration then quickly decays and becomes lower compared to the non-coupling case. And the lowest concentration occurs at the margin of the imperfection. This result agrees with the above discussion about the hydrostatic stress. The compressive hydrostatic stress increases the chemical potential of oxygen, which drives oxygen diffusion from the compressed region to the tensed region. In other words, the local tensile stress attracts oxygen diffusion, while compressive stresses drive oxygen away. As influenced by the stress regulation, the oxygen influx along the BC–TGO interface is not homogeneous any more. On the other

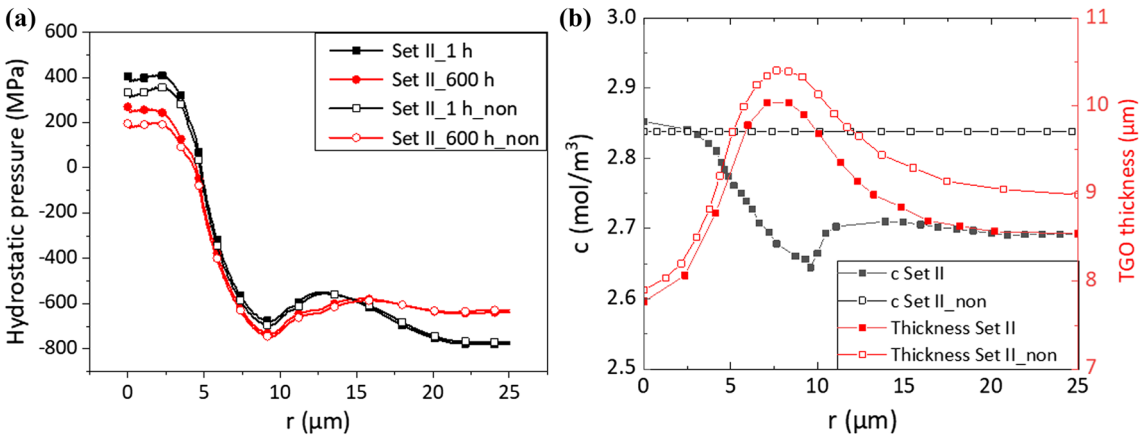

Figure 6 **a** Hydrostatic stress for Set II; **b** oxygen concentration along the upper boundary of TGO (original TC–BC interface) and TGO thickness distribution along the interface after 600 h. Note that for all three figures, 'r' denotes the distance to the centre of the concave.

hand, large compressive stress at the interface between concave and flat regions, see Fig. 6a, slows down the oxygen diffusion into TGO layer, resulting in a low oxygen concentration at that interface, see Fig. 6b. The maximum thickness of TGO appears at the junction of the concave and flat regions, as shown in Fig. 6b, while the minimum thickness of TGO appears at the centre of the concave region. This contradicts the intuitive perception that TGO would be thicker in regions where oxygen concentration is higher.

The counterintuitive result is caused by the non-homogeneous oxygen diffusion around the geometrical imperfection. As shown in Fig. 7, the horizontal gradient of the oxygen chemical potential caused by the interface imperfection keeps driving oxygen to the region between concave and flat regions, even though this region is under high compressive stress. Also, although the oxygen concentration is high around the centre of concave imperfection and low around the concave imperfection margin, see Fig. 6b, the outward oxygen flux slows down the further built-up of oxygen concentration at the concave imperfection centre, suppressing the growth of oxide there while accelerating the accumulation of the oxygen in the concave imperfection margin, as shown in Fig. 6b. The TGO thickness plotted in Fig. 6b shows a thicker TGO layer formed at the region between concave and flat regions, indicating that the influence of the geometric curvature has overcome the stress regulation effect on oxygen diffusion.

Note that, in the coupling model, the difference in chemical potential of oxygen caused by stress is limited by the magnitude of the stress in the TGO.

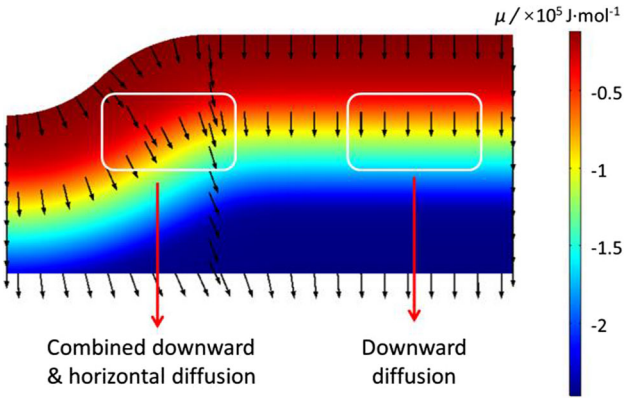

Figure 7 Chemical potential of oxygen and the associated oxygen flux in TBCs (black arrows) at the 100th hour of oxidation time.

Thus, the difference in TGO thickness and other quantities like stress between the coupling and non-coupling model is limited in TBCs. In other words, the coupling effect has limited impact on TGO growth kinetics.

Stress-regulated morphology of TGO layer

As shown in Fig. 6a, large compressive stresses could be present at the marginal region of the concave imperfection. These stresses contribute to the morphology of the TGO layer in two aspects. Firstly, the out-of-plane displacement which releases the large compressive stresses will cause the amplitude change of the TC–TGO interface. Therefore, the enlarging of the imperfection is concomitant with the oxidation process. Specifically, the amplitude of the concave imperfection would grow increasingly large, as

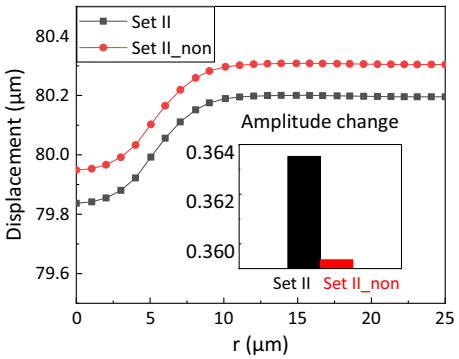

Figure 8 Displacement of the TGO–TC interface and the amplitude change of the concave imperfection along the interface at high temperature.

shown in Fig. 8. At high temperature, the amplitude change of the concave imperfection is about 0.36 μm, which is much more obvious than the short-term exposure reported previously (0.04 μm after a one-hour cycle) [24].

Secondly, this amplitude change could induce local tensile stress around the concave imperfection [56]. Large tensile stresses, which are sufficient to initiate micro-cracks in the ceramic top coat and peak at the flanks of BC protuberances, occur in the region above the concave imperfection, as shown in Fig. 9. These stresses, in accordance with previous studies [16], drive the initiation of micro-cracks in the TC [1]. Once initiated, the cracks provide transport path for oxygen which leads to formation of the mixed oxide [21]. Note that the σ_z during the oxidation process exhibits little change, mainly because of the plastic flow of the BC, which releases the oxidation-induced stresses.

Conclusions

In this paper, a chemo-transport-mechanics model has been developed to predict the growth kinetics of thermally grown oxide (TGO) and the resultant displacement and stress fields in thermal barrier coatings (TBCs). The following conclusions are drawn:

1. The diffusion of oxygen has major effect on TGO growth kinetics. The formed oxide acts as a diffusion barrier to impede TGO growth in the oxidation front due to its lower diffusion coefficient of oxygen. For the first time, our model considers the difference in the diffusion coefficient of oxygen between BC and TGO and clarifies the retarding effect of existing TGO on oxygen diffusion.
2. Geometrical imperfection (i.e. concave morphology) causes the horizontal component of the gradient of the chemical potential of oxygen, which governs the local growth of the TGO. The chemo-mechanics coupling has limited effect on TGO growth kinetics in the studied TBCs, due to the low magnitude of both the stress and the partial molar volume.
3. During the oxidation process, the amplitude of the concave portion enlarges continuously by 0.36 μm after 600-h exposure due to compressive stress in TGO. Tensile stresses up to 600 MPa are predicted in the region above the concave portion of the top coat, with the maximum occurring in the flank of the imperfection.

Finally, it should be noted that the model developed in this study can be also used to predict the

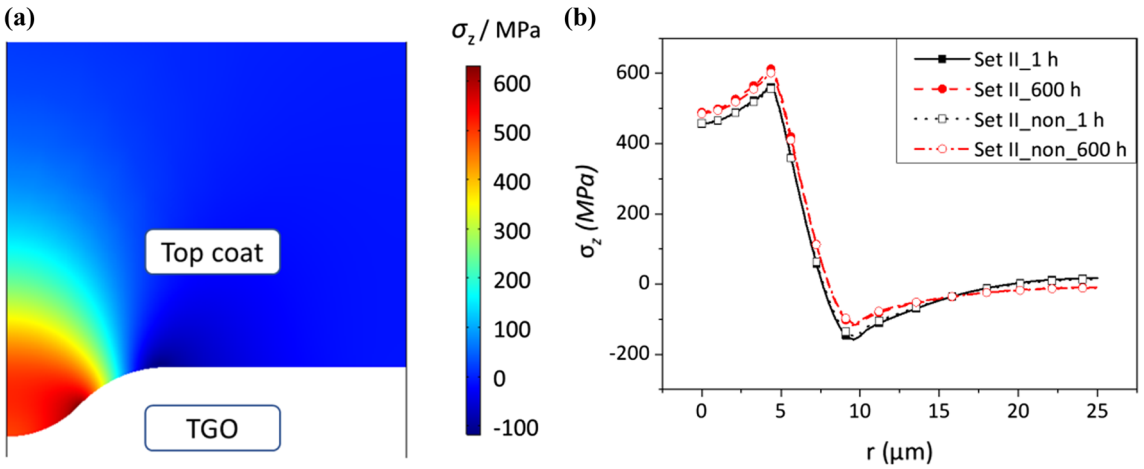

Figure 9 σ_z stress: **a** contour. **b** Along the interface in the top coat and its evolution.

chemo-transport-mechanics coupling behaviour of other material systems and potential strong coupling effects can be examined.

Acknowledgements

This work is supported by NSFC (11472204 and 1171101165) and the Fundamental Research Funds for the Central Universities.

Compliance with ethical standards

Conflict of interest The authors declare no conflict of interest.

References

[1] Padture NP, Gell M, Jordan EH (2002) Thermal barrier coatings for gas-turbine engine applications. Science 296:280–284

[2] Evans AG, Mumm DR, Hutchinson JW et al (2001) Mechanisms controlling the durability of thermal barrier coatings. Prog Mater Sci 5:505–553

[3] Clarke DR, Oechsner M, Padture NP (2012) Thermal-barrier coatings for more efficient gas-turbine engines. MRS Bull 37:891–898

[4] Xu R, Fan XL, Zhang WX et al (2013) Effects of geometrical and material parameters of top and bond coats on the interfacial fracture in thermal barrier coating system. Mater Des Complete 47:566–574. https://doi.org/10.1016/j.matdes.2012.12.053

[5] Xu R, Fan X, Wang TJ (2016) Mechanisms governing the interfacial delamination of thermal barrier coating system with double ceramic layers. Appl Surf Sci C 370:394–402

[6] Jiang P, Fan X, Sun Y et al (2018) Bending-driven failure mechanism and modelling of double-ceramic-layer thermal barrier coating system. Int J Solids Struct 130–131:11–20

[7] Sun Y, Li J, Zhang W, Wang TJ (2013) Local stress evolution in thermal barrier coating system during isothermal growth of irregular oxide layer. Surf Coat Technol 216:237–250

[8] Sun Y, Zhang W, Li J, Wang TJ (2013) Local stress around cap-like portions of anisotropically and nonuniformly grown oxide layer in thermal barrier coating system. J Mater Sci 48:5962–5982. https://doi.org/10.1007/s10853-013-7393-7

[9] Fan XL, Qin WJ (2011) Stress distribution in the vicinity of thermally grown oxide of thermal barrier coatings. Adv Mater Res 160–162:721–725

[10] Fan XL, Zhang WX, Wang TJ, Sun Q (2012) The effect of thermally grown oxide on multiple surface cracking in air plasma sprayed thermal barrier coating system. Surf Coat Technol 208:7–13

[11] Su L, Zhang W, Sun Y, Wang TJ (2014) Effect of TGO creep on top-coat cracking induced by cyclic displacement instability in a thermal barrier coating system. Surf Coat Technol C 254:410–417

[12] Xu R, Fan XL, Zhang WX, Wang TJ (2014) Interfacial fracture mechanism associated with mixed oxides growth in thermal barrier coating system. Surf Coat Technol 253:139–147

[13] Li B, Fan X, Zhou K, Wang TJ (2017) Effect of oxide growth on the stress development in double-ceramic-layer thermal barrier coatings. Ceram Int 43:14763–14774

[14] Lv J, Fan X, Li Q (2017) The impact of the growth of thermally grown oxide layer on the propagation of surface cracks within thermal barrier coatings. Surf Coat Technol 309:1033–1044

[15] Evans HE (2011) Oxidation failure of TBC systems: an assessment of mechanisms. Surf Coat Technol 206:1512–1521

[16] Busso EP, Wright L, Evans HE et al (2007) A physics-based life prediction methodology for thermal barrier coating systems. Acta Mater 55:1491–1503

[17] Rabiei A, Evans AG (2000) Failure mechanisms associated with the thermally grown oxide in plasma-sprayed thermal barrier coatings. Acta Mater 48:3963–3976

[18] Evans AG, He MY, Hutchinson JW (2001) Mechanics-based scaling laws for the durability of thermal barrier coatings. Prog Mater Sci 46:249–271

[19] Fan XL, Xu R, Zhang WX, Wang TJ (2012) Effect of periodic surface cracks on the interfacial fracture of thermal barrier coating system. Appl Surf Sci 258:9816–9823

[20] Busso EP, Qian ZQ, Taylor MP, Evans HE (2009) The influence of bondcoat and topcoat mechanical properties on stress development in thermal barrier coating systems. Acta Mater 57:2349–2361

[21] Busso EP, Evans HE, Qian ZQ, Taylor MP (2010) Effects of breakaway oxidation on local stresses in thermal barrier coatings. Acta Mater 58:1242–1251

[22] He MY, Hutchinson JW, Evans AG (2002) Large deformation simulations of cyclic displacement instabilities in thermal barrier systems. Acta Mater 50:1063–1073

[23] Karlsson AM, Hutchinson JW, Evans AG (2002) A fundamental model of cyclic instabilities in thermal barrier systems. J Mech Phys Solids 50:1565–1589

[24] Karlsson AM, Xu T, Evans AG (2002) The effect of the thermal barrier coating on the displacement instability in thermal barrier systems. Acta Mater 50:1211–1218

[25] Kang K-J, Hutchinson JW, Evans AG (2003) Measurement of the strains induced upon thermal oxidation of an alumina-forming alloy. Acta Mater 51:1283–1291

[26] He MY, Hutchinson JW, Evans AG (2003) Simulation of stresses and delamination in a plasma-sprayed thermal barrier system upon thermal cycling. Mater Sci Eng A 345:172–178

[27] Karlsson AM, Hutchinson JW, Evans AG (2003) The displacement of the thermally grown oxide in thermal barrier systems upon temperature cycling. Mater Sci Eng A 351:244–257

[28] Xu T, He MY, Evans AG (2003) A numerical assessment of the durability of thermal barrier systems that fail by ratcheting of the thermally grown oxide. Acta Mater 51:3807–3820

[29] Zhou H (2010) Stress-diffusion interaction during oxide scale growth on metallic alloys. Ph.D. Dissertation. Georgia Institute of Technology

[30] Loeffel K, Anand L (2011) A chemo-thermo-mechanically coupled theory for elastic–viscoplastic deformation, diffusion, and volumetric swelling due to a chemical reaction. Int J Plast 27:1409–1431

[31] Loeffel K, Anand L, Gasem ZM (2013) On modeling the oxidation of high-temperature alloys. Acta Mater 61:399–424

[32] Chen L, Yueming L (2018) A coupled mechanical-chemical model for reflecting the influence of stress on oxidation reactions in thermal barrier coating. J Appl Phys 123:215305

[33] Suo Y, Shen S (2015) Coupling diffusion–reaction–mechanics model for oxidation. Acta Mech 226:3375–3386

[34] Wang T, Fan XL et al (2016) The stresses and cracks in thermal barrier coating system: a review. Chin J Solid Mech 37(6):477–517

[35] Mura T (1987) Micromechanics of defects in solids, 2nd edn. Springer, Dordrecht

[36] Panicaud B, Grosseau-Poussard JL, Dinhut JF (2008) General approach on the growth strain versus viscoplastic relaxation during oxidation of metals. Comput Mater Sci 42:286–294

[37] Suo Y, Shen S (2013) General approach on chemistry and stress coupling effects during oxidation. J Appl Phys 114:164905

[38] Suo Y, Yang X, Shen S (2015) Residual stress analysis due to chemomechanical coupled effect, intrinsic strain and creep deformation during oxidation. Oxid Met 84:413–427

[39] Panicaud B, Grosseau-Poussard JL, Dinhut JF (2006) On the growth strain origin and stress evolution prediction during oxidation of metals. Appl Surf Sci 252:5700–5713

[40] Maharjan S, Zhang XC, Xuan FZ et al (2011) Residual stresses within oxide layers due to lateral growth strain and creep strain: analytical modeling. J Appl Phys 110:063511

[41] Tolpygo VK, Dryden JR, Clarke DR (1998) Determination of the growth stress and strain in α-Al2O3 scales during the oxidation of Fe–22Cr–4.8Al–0.3Y alloy. Acta Mater 46:927–937

[42] Ruan JL, Pei Y, Fang D (2012) Residual stress analysis in the oxide scale/metal substrate system due to oxidation growth strain and creep deformation. Acta Mech 223:2597–2607

[43] Ruan JL, Pei Y, Fang D (2013) On the elastic and creep stress analysis modeling in the oxide scale/metal substrate system due to oxidation growth strain. Corros Sci 66:315–323

[44] Hsueh CH, Evans AG (1983) Oxidation induced stresses and some effects on the behavior of oxide films. J Appl Phys 54:6672–6686. https://doi.org/10.1063/1.331854

[45] Pilling N, Bedworth RJ (1923) The oxidation of metals at high temperatures. J Inst Met 29:529–582

[46] Li JCM (1981) Chemical potential for diffusion in a stressed solid. Scr Metall 15:21–28

[47] Reynolds O (1903) Papers on mechanical and physical subjects, vol 3. Cambridge University Press, Cambridge

[48] Devereux OF (1983) Topics in metallurgical thermodynamics: solutions manual. Wiley-Interscience, New York

[49] Shillington EAG, Clarke DR (1999) Spalling failure of a thermal barrier coating associated with aluminum depletion in the bond-coat. Acta Mater 47(4):1297–1305

[50] Wang L, Yang JS, Ni JX et al (2016) Influence of cracks in APS-TBCs on stress around TGO during thermal cycling: a numerical simulation study. Surf Coat Technol 285:98–112

[51] Quested PN, Brooks RF, Chapman L et al (2009) Measurement and estimation of thermophysical properties of Nickel based superalloys. Mater Sci Technol 25:154–162

[52] Jiang W, Zhang Y-C, Zhang WY et al (2016) Growth and residual stresses in the bonded compliant seal of planar solid oxide fuel cell: Thickness design of window frame. Mater Des C 93:53–62

[53] Cheng J, Jordan EH, Barber B, Gell M (1998) Thermal/residual stress in an electron beam physical vapor deposited thermal barrier coating system. Acta Mater 46:5839–5850

[54] Martena M, Botto D, Fino P et al (2006) Modelling of TBC system failure: stress distribution as a function of TGO thickness and thermal expansion mismatch. Eng Fail Anal 13:409–426

[55] Richards BT, Young KA, de Francqueville F et al (2016) Response of ytterbium disilicate–silicon environmental barrier coatings to thermal cycling in water vapor. Acta Mater 106:1–14

[56] Knipe K, Manero Ii A, Siddiqui SF et al (2014) Strain response of thermal barrier coatings captured under extreme engine environments through synchrotron X-ray diffraction. Nat Commun 5:4559